An Experimental Study of Steam-Assisted Gravity Drainage

Kai Sheng and **Ryosuke Okuno,** University of Texas at Austin; **Muhammad Imran,** Saskatchewan Research Council; and **Tomomi Yamada,** Japan Canada Oil Sands Ltd.

Summary

In this paper we present a large-scale experimental study of the compositional effect on produced bitumen properties in steam-assisted gravity drainage (SAGD). The SAGD experiment used a sandpack in the cylindrical pressure vessel that was 1.22 m in length and 0.425 m in internal diameter. The pore volume of the sandpack was 58 L, and the porosity and permeability were 0.33 and 5.5 darcy, respectively. The sandpack was initially saturated with 93% bitumen and 7% deionized water.

The SAGD experiment after preheating was operated mostly at a steam injection rate of 35 cm^3/min (cold-water equivalent) at 3,600 kPa (244°C). The produced fluids (gas, oil, and water) were analyzed; for example, 10 oil samples were analyzed in terms of carbon number distribution (CND), the asphaltene content, density, and viscosity to investigate the compositional change of the produced bitumen. After the experiment, the sandpack was excavated, and samples were taken for analysis of solid, water, oil, asphaltene, and sulfur contents. Experimental data (e.g., propagation of a steam chamber and production of oil and water) were history matched using a numerical reservoir simulator.

The produced bitumen was lighter and contained 1- to 5-wt% less asphaltenes than the original bitumen. Also, the remaining oil inside the steam chamber contained 6-wt% more asphaltenes. As a result, the produced bitumen was 1- to 6-kg/m^3 less dense than the original bitumen. This is an increase in API gravity from the original 7.9° to 8.6°. In the actual operations, bitumen is diluted with condensate to decrease the oil viscosity for pipeline shipping. This decrease in bitumen density corresponds to a decrease of the diluent cost by 5 to 10%. The produced bitumen became less dense with increasing steam-chamber volume.

Results were history matched with a simulation model that considers capillary pressures to properly model the mixed flow regimes of oil/water countercurrent and cocurrent flow with an expanding steam chamber. The history-matched simulation indicated that the progressively decreasing density of the produced bitumen can be attributed to the vaporization of the relatively volatile components in the remaining oil and condensation of those components near the chamber edge.

Introduction

SAGD has been widely used for bitumen recovery in Canada. A pair of horizontal wells are drilled near the bottom of the reservoir in SAGD. Steam is injected through the upper well into the reservoir. The reservoir oil in SAGD is often immobile at the initial conditions but is made mobile by the heat (latent and sensible) released from the high-quality steam injected. The steam-saturated volume, which is called the steam chamber, expands as the oil production continues. The mobilized oil along with condensed water is produced through the lower horizontal well because of a large density difference between the oil and vapor phases inside and near the edge of a steam chamber.

SAGD is one of the successful applications of steam injection into heavy oil reservoirs. It has various mechanisms in common with the traditional steamflooding; for example, the viscosity decrease by heat, gravity-driven oil flow, and in-situ upgrading. The in-situ upgrading includes distillation and deasphaltening by solvent according to Ovalles (2019), who defined in-situ upgrading of heavy oil and bitumen as the permanent change to the subsurface heavy oil or bitumen through physical or chemical reactions. This paper is concerned mainly with the distillation of volatile components, one of the in-situ upgrading mechanisms for SAGD (Prats 1982; Ovalles 2019).

The distillation mechanism has been well known for steamflooding, by which the local displacement of oil is enhanced (Prats 1982; Ovalles 2019). Willman et al. (1961) observed in their steam-drive coreflooding tests that the oil recovery could be substantially improved by the distillation of volatile fractions in the oil stripped by the injected steam. Their oil samples were synthesized by mixing a high fraction of naphtha, which was 100% distillable, with heavy crudes with approximately 20°API. Prats (1982) commented on the results of Willman et al. (1961) that distillation should take place in actual heavy oil and bitumen recovery by steam because they are mixtures of hydrocarbons with a wide range of carbon number. Duerksen and Hsueh (1983) reported that the distillation yield by steam for a crude oil of 10°API could be up to 20% at low pressures. Their porous medium was a one-dimensional core with approximately 600- to 800-μm sands. Similar distillation experiments were performed by Wu and Brown (1975) and Liu et al. (2018). Their experiments were designed for the steam to sufficiently take away distillables without oil production in a pressurized cell. There are only a limited number of experimental studies about the compositional change of bitumen associated with the distillation of volatiles in realistic operation conditions and pore sizes for SAGD. Al-Murayri et al. (2016a, 2016b) showed a slightly elevated asphaltene weight percentage in the vicinity of wellbore after the SAGD and solvent-assisted SAGD (SA-SAGD) tests in their two-dimensional sandpacks. Mukhametshina and Hascakir (2014) showed slightly lower viscosity of the produced bitumen in comparison to the original bitumen in their SAGD experiment.

The distillation of volatiles has been studied as one of the key mechanisms in SA-SAGD (Dong 2012; Hosseininejad Mohebati et al. 2012; Keshavarz et al. 2014, 2015; Sheng et al. 2018; Venkatramani and Okuno 2018). When the injected solvent condenses near the chamber edge and mixes with bitumen, the diluted oil drains under gravity, making the remaining oil phase solvent rich. As the steam chamber expands, the solvent in the remaining oil vaporizes and recondenses near the chamber edge, resulting in a small amount of residual bitumen. The distillation of volatile components in bitumen can be also important for practical SAGD operations because it affects the produced oil properties (e.g., density and viscosity). For the same reason, the collected bitumen sample should be corrected for the distillation effect for SAGD studies. A recent simulation study with the bitumen characterized as multiple components has

Original SPE manuscript received for review 8 May 2020. Revised manuscript received for review 29 June 2020. Paper (SPE 200867) peer approved 14 August 2020.

shown that the light end of bitumen accumulated near the edge of a steam chamber and resulted in the produced bitumen that was less dense than the original bitumen.

Use of a large-scale physical model is advantageous for a mechanistic study of SAGD and its variants, such as SA-SAGD. Achieving semisteady-state production is important for analysis of such transient experimental data, but often difficult at laboratory-scale dimensions because of a limited amount of oil in place and a large amount of heat loss. In this research, a SAGD experiment was performed with a large-scale physical model at Saskatchewan Research Council (SRC), Regina, Saskatchewan, Canada. The sandpack used for the experiment had a pore volume of 58 L with a porosity of 33%, resulting in one of the largest laboratory-scale experiments for SAGD.

Laboratory experiments have been performed to investigate mechanisms of efficient oil recovery in SAGD and SA-SAGD. Visual observations of steam injection processes provided insights into the oil recovery mechanisms at relatively low operating pressures in many two-dimensionalvisual-cell SAGD studies (Sasaki et al. 1999; Kim et al. 2017; Liu et al. 2018; Xu et al. 2018). Although the insulation often makes it impossible to have visual windows, it helps investigate the mechanisms of SAGD and SA-SAGD at more realistic operation conditions. Such experiments are frequently used to test new conditions and solvents or to compare among several solvents for SA-SAGD and compare their performance with SAGD. For example, Nasr et al. (2003) compared a variety of *n*-alkane solvents and solvent mixtures and concluded that hexane was the best solvent as an additive to enhance the SAGD production rate for Athabasca bitumen. Hosseininejad Mohebati et al. (2012) tested different pressures to find out the optimum operating pressure for hexane compared with SAGD. Ayodele et al. (2009) and Ivory et al. (2008) tested the applicability of diluents as additives to steam for low-pressureSA-SAGD, and Khaledi et al. (2012) tested diluents for high-pressureSA-SAGD operations. Li et al. (2011) compared the performance of SA-SAGD using heptane, xylene, and mixtures of the two solvents, and Mukhametshina and Hascakir (2014) compared hexane and toluene in SA-SAGD. Al-Murayri et al. (2016a,b) tested naphtha and condensates in SA-SAGD to investigate whether those solvents improved SAGD and whether it resulted in any asphaltene precipitation in the experiment. Water-soluble solvents have also been tested for SA-SAGD, such as dimethyl ether (Haddadnia et al. 2018) and ethyl acetate (Zirahi et al. 2020).

The objective of this paper is to present an experimental study of the effect of distillation, which is one of the in-situ upgrading mechanisms, on the produced oil properties during SAGD using a large-scale physical model. The experiment was performed using a bitumen sample taken from a SAGD operation site without mixing it with solution gas; therefore, the results in this research would be an underestimation of the distillation effects on the produced oil properties. The CND of the produced bitumen samples and the asphaltene contents of the remaining oil and the produced bitumen were analyzed and compared with the original bitumen. To the authors' knowledge, this is the first time the distillation mechanism was experimentally studied for SAGD-type flow configuration with no solvent injection. Experimental data were history matched by a numerical reservoir simulator to study the compositional effect (i.e., distillation) on bitumen recovery. Although it is not the primary objective, this paper also demonstrates the mixed flow regimes of counter- and cocurrent flow during SAGD based on history-matched simulation.

The subsequent sections first present the experimental setup and operational procedures, second the experimental results, third the history matching and its analysis, and finally, the key conclusions of this research.

SAGD Experimental Setup and Operations

This section presents an overview of the physical model apparatus, properties of the oil sample used for the experiment, and the packing and fluid saturation of the physical model. It also describes the procedures for the preheating, SAGD experiment, ramp-down, cooling, fluid sampling, and excavation of the sandpack.

Experimental Apparatus. **Fig. 1** shows a schematic of the SAGD experimental setup (SRC). It consists of the following:

- A carbon steel cylindrical pressure vessel that is 1.22 m in length and 0.425 m in internal diameter.
- Carbon steel flanges designed for the insertion of two horizontal wells and a grid of thermocouples.
- Perforated injection and production wells that are 0.0254 m in diameter.
- Two 1.22-m heaters in the injection and production wells equipped with thermocouples measuring heater surface temperature.
- A grid of thermocouples on five vertical planes along the model length, giving a total of 95 temperature data points (i.e., 19 thermocouples on each vertical plane).
- Six band heaters around the cylindrical vessel to control heat losses (three heaters for the top half and the other three for the bottom half of the vessel).
- High-pressure injection pumps (up to 34,000 kPa).
- A pressurized and insulated production system with two 18-L capacity production tanks.
- A steam generator (up to 15 kW).
- An online gas chromatography to analyze gas composition.
- A wet gas meter to measure produced gases.

Two horizontal wells were vertically stacked at 0.12 and 0.04 m from the bottom of the cylindrical pressure vessel as shown in **Fig. 2.** Both wells were covered by a stainless-steel sieve to prevent sand production during the experiment. The upper injection well was equipped with a centralized inline heater, and a five-point thermocouple measured temperatures on the surface of the heater. The production well was equipped with a three-segment inline heater. Each heater had its surface thermocouple to control the heat distribution along the production well.

The physical model had 19 multipoint thermocouples on five vertical planes that were equally spaced along the length of the model (Fig. 2b). The model was also equipped with band heaters, surrounding the cylindrical pressure vessel to heat the entire vessel and control heat losses. Furthermore, the physical model and injection/production lines were insulated to decrease heat losses. Three pressure gauges monitored the pressure change along the sandpack (Fig. 2).

Oil Properties. The bitumen sample for this experiment was prepared from the emulsion sample obtained from Athabasca thermal operations, Alberta, Canada. The original emulsion sample had a water cut of approximately 75% by weight.

Properties of the cleaned Athabasca bitumen were measured before the SAGD experiment. The molecular weight is 560 g/mol, and the density is 1015 kg/m^3 at 15°C and atmospheric pressure. **Table 1** shows the saturates, asphaltenes, resins, and aromatics (SARA) composition. **Table 2** shows the initial dead oil densities and viscosities at different temperatures. A Brookfield viscometer was used for the viscosity measurements. The oil densities were measured using a commercial digital density analyzer.

The CND of the bitumen was analyzed using gas chromatography as shown in **Fig. 3.** The lightest component detected in the bitumen sample was C_{11}. The gas chromatography measured CNs up to 120. The peaks of the CND curves appeared at approximately C_{20}.

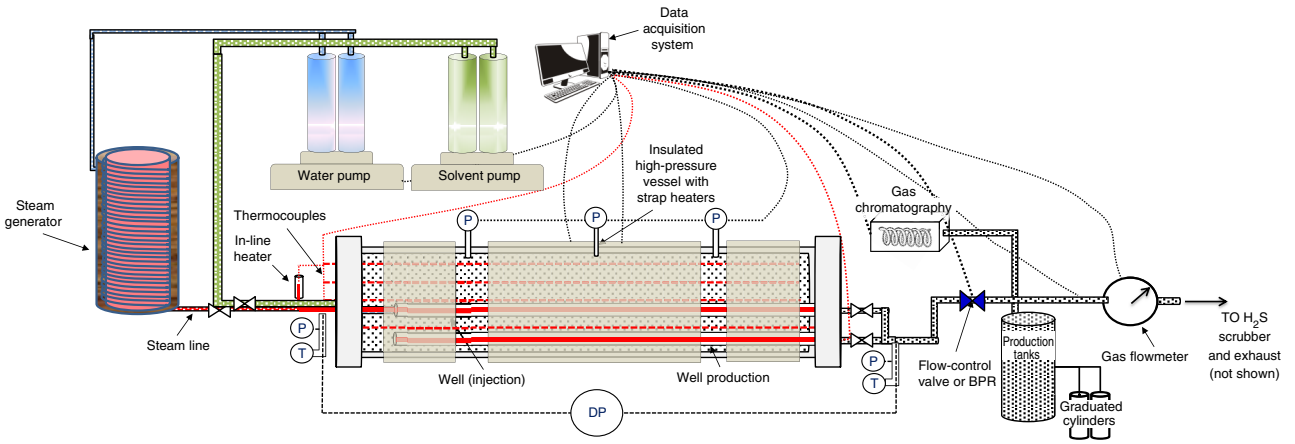

Fig. 1—Schematic of the SAGD experimental setup. BPR, DP, P, and T in the figure are backpressure regulator, pressure transducer for pressure drop measurements, pressure gauge, and temperature gauge, respectively. H_2S is hydrogen sulfide.

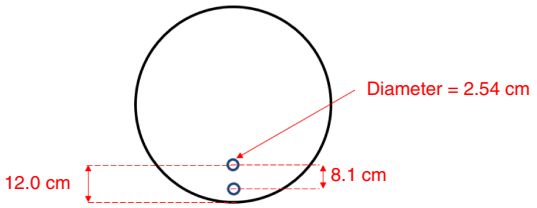

(a) Locations of the horizontal wells on a vertical cross-section.

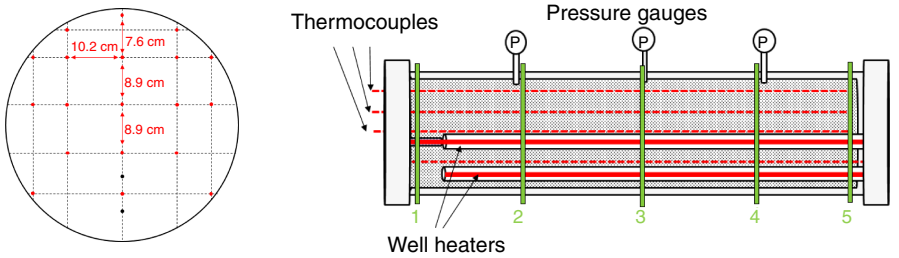

(b) Locations of the thermocouples in the sandpack. (Red dots: thermocouples; black dots: horizontal wells)

Fig. 2—Locations of the horizontal wells and thermocouples in the sandpack.

Properties	Values
Saturates (wt%)	18.79
Aromatics (wt%)	38.98
Resins (wt%)	17.69
Asphaltene (wt%)	17.82
Unrecovered (wt%)	6.72

Table 1—SARA analysis of the dead bitumen. The SARA concentrations do not sum up to one because part of the light fractions vaporized and part of the heavy fractions remained in the column (unrecovered).

Properties	Values
Density at 15°C (kg/m^3)	1015.24
Density at 40°C (kg/m^3)	999.42
Density at 80°C (kg/m^3)	974.10
Viscosity at 15°C (cp)	1,000,000
Viscosity at 40°C (cp)	24,000
Viscosity at 80°C (cp)	675

Table 2—Initial dead oil densities and viscosities at different temperatures.

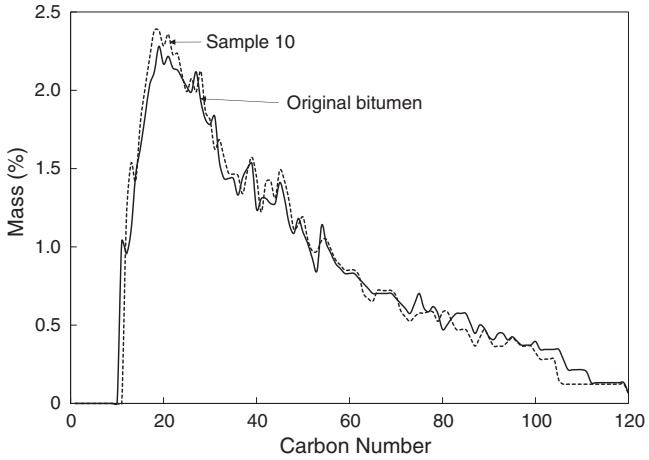

Fig. 3—Carbon number distribution of the original bitumen (solid) and Sample 10 (dashed).

Experiment Procedures. ***Model Packing and Oil Saturation.*** The cylindrical pressure vessel was dry-packed with 314.861 kg of sand, representing unconsolidated sands. **Fig. 4** shows the grain-size distribution. The packing was completed after installing one of the flanges of the cylindrical model along with the injection and production wells and the grid of thermocouples. Once it was packed and compacted, the model was sealed by installing the second flange at the open end of the cylindrical model. The model was evacuated to test the cylindrical model for leakage. Then, the model was filled with 57.95 L deionized water. The water imbibition was done at room temperature (22 to 23°C). The bulk volume of the pressure vessel was 175.67 L after correction for well and thermocouple volumes, resulting in the porosity of the sandpack of 32.99%. For bitumen saturation, the entire physical model was heated to approximately 75°C. Heated bitumen was injected into the imbibition ports at the bottom of the vessel, displacing water into the ports at the top of the model. The amount of water produced during bitumen saturation was 53.95 L, giving an oil saturation of 93.11%. The permeability was measured to be 5.5 D.

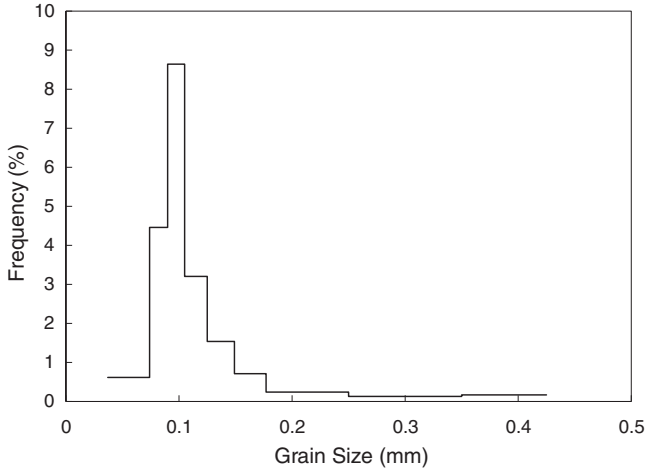

Fig. 4—Grain-size distribution of the sandpack.

Model Preheating. After fluid saturation of the model, the preheating stage began by turning on the injection and production well heaters. The injection well's inline heater was controlled by internal temperatures and different set points were assigned to gradually preheat the model for at least 24 hours. The production system heaters were also turned on at a set point of approximately 80°C. The heat losses were controlled by turning on the top band heaters during the preheating stage. The injection well and production well heaters were set to 125°C for 24 hours.

SAGD Experiment. After the preheating stage, steam of 100% quality was injected into the sandpack through three injection points along the injection well throughout the experiment. Steam was injected at a constant rate of 35 cm^3/min [cold-water equivalent (CWE)] at 3,600 kPa and 244°C. The production of fluids began shortly after the start of steam injection when the production side valves were opened to production receiving pumps. The production pumps were initially set at 40 cm^3/min. After the start of steam injection, the injection well heater set point was increased gradually over the next 10 hours from 125°C to approximately 265°C to ensure that 100% quality steam was injected into the sandpack. During the first day of the SAGD experiment, only top band heaters were running and were controlled based on the temperature thermocouple points inside of the metal shell in the uppermost section of the sandpack. This was to avoid the direct breakthrough of steam during the beginning stage of the experiment.

On the second day of the SAGD experiment, the bottom band heaters were turned on, and the system pressure was decreased to 3,500 kPa. The reason for starting the bottom band heaters was to control heat losses from the bottom of the sandpack, which facilitated the expansion of a steam chamber. The injection well heater set point was also gradually changed to ensure 5 to 10°C above the steam saturation temperature (approximately 242°C). Similarly, the production well heater set point was increased gradually from 125°C to approximately 240°C for 2 days.

On the fifth day of the SAGD experiment, the steam injection rate was increased from 35 to 50 cm^3/min while maintaining the same system pressure setting of 3,500 kPa. The injection well heater set point was decreased slightly to 260°C. Both top and bottom band heaters continued running until the end of the SAGD experiment.

To summarize, the SAGD experiment after preheating was operated in three main stages. During Stage 1, steam was injected at a pressure and temperature of 3,600 kPa, and 244°C, respectively, and at a rate of 35 cm^3/min (CWE), but there was no heat loss control on the bottom side of the sandpack. Stage 1 lasted for 1 day. In Stage 2, the steam rate was set at 35 cm^3/min (CWE), and the bottom band heaters were turned on. Stage 2 ran for 3 days. In Stage 3, the injection rate was increased from 35 to 50 cm^3/min with the bottom band heaters on for 7.2 days.

Ramp-Down/Cooling Stage. Once the SAGD experiment was completed, the system was prepared for the ramp-down/cooling phase. Steam injection pumps were stopped, and the injection valves and main production valves were closed. The injection well and production well heaters were turned off. The top and bottom band heaters were turned off as well. Finally, the gas chromatograph sampling system was stopped.

The model system was then prepared for evacuation of the sandpack from the top ports of the vessel. The vacuum pump ran initially for 8 hours. Nitrogen purge started, but the hydrogen sulfide (H_2S) concentration in the purged gas was still greater than 10 ppm. Therefore, the sandpack was evacuated for additional 4 hours. Nitrogen purge was restarted on the sandpack until the H_2S concentration was less than 10 ppm.

Handling of Produced Fluids. The SAGD operating parameters were controlled by the data acquisition system developed by SRC. During the experiment, once a production tank was filled, the production flow was directed toward the second production tank. The full production tank was then drained by placing a graduated cylinder (collection vessel) under the drain line of the production tank. The produced gas passed through a condenser to capture water vapor. A wet flowmeter was used to measure the amount of produced gas. Then, the produced gas passed through the online gas chromatograph to analyze the composition. Finally, the produced gas was vented through scrubbers.

The produced liquid phase was analyzed to measure the amounts of water and bitumen. The cumulative water injection, water production, and bitumen production were measured and recorded during the experiment. A total of 10 fluid samples were taken during the experiment, for which the CND, asphaltene content, density, and viscosity were measured at different temperatures to monitor the compositional change of the produced bitumen.

Post-Run: Degassing and Model Excavation. Once the SAGD experiment was performed, the experimental model was cooled down to room temperature. Then, the model was excavated from both ends (injection and production) for a total of eight segments. Samples were taken from each segment for Dean-Stark analysis. Solids, water, and oil content, and asphaltene and sulfur content were measured for the collected samples.

Experimental Results and Discussion

Fig. 5 shows the history of water injection, water production, and bitumen production. Steam was initially injected at 35 cm^3/min (CWE) and then increased to 50 cm^3/min at approximately 7,200 minutes (5.0 days), as shown by the slope change in this figure. The bitumen production was slower before 3,000 minutes and became more rapid when the bottom heater was turned on to control heat losses. The ultimate oil recovery was 47.074 L, which is approximately 87% original oil in place.

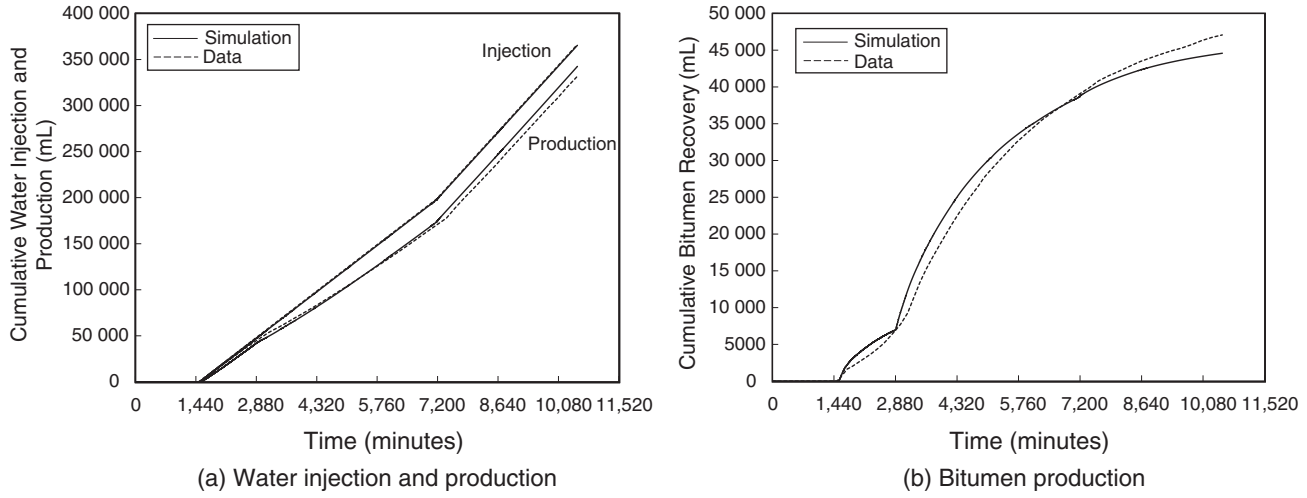

Fig. 5—Cumulative water injection, water production, and bitumen production from the experiment and numerical simulation.

The temperature data were processed to estimate the propagation of the steam chamber boundary. A temperature surface was constructed by using the temperature readings from the 103 thermometers, and then the steam chamber edge was estimated by the isothermal contour of the saturated steam temperature at 3,500 kPa, which is 242°C. **Fig. 6** shows the approximate boundary of the steam chamber (the contour for 242°C) and four other contours from 225 to 240°C, on each vertical plane at the end of each day. The steam chamber expanded much more rapidly on planes from 1 to 3 than planes 4 and 5, indicating greater heat losses on the production end of the experimental setup.

Table 3 reports the density, the cumulative weight percentage up to C_{50}, and the asphaltene content of the 10 bitumen samples collected from the production well, along with the time these samples were taken. Fig. 3 shows the CNDs measured for Sample 10 and the original bitumen. The CND of Sample 10 below C_{50} was slightly higher than that of the original bitumen and slightly lower in the region greater than C_{50}. **Fig. 7** compares the cumulative weight percentage up to C_{50} for all the produced fluid samples and the original bitumen. The fractions lighter than C_{50} of the produced bitumen samples were 0.7- to 2.1-wt% greater than that of the original bitumen. As steam chamber expands, the greater difference was observed between the original bitumen and the produced fluid in weight percentage of the fractions lighter than C_{50}.

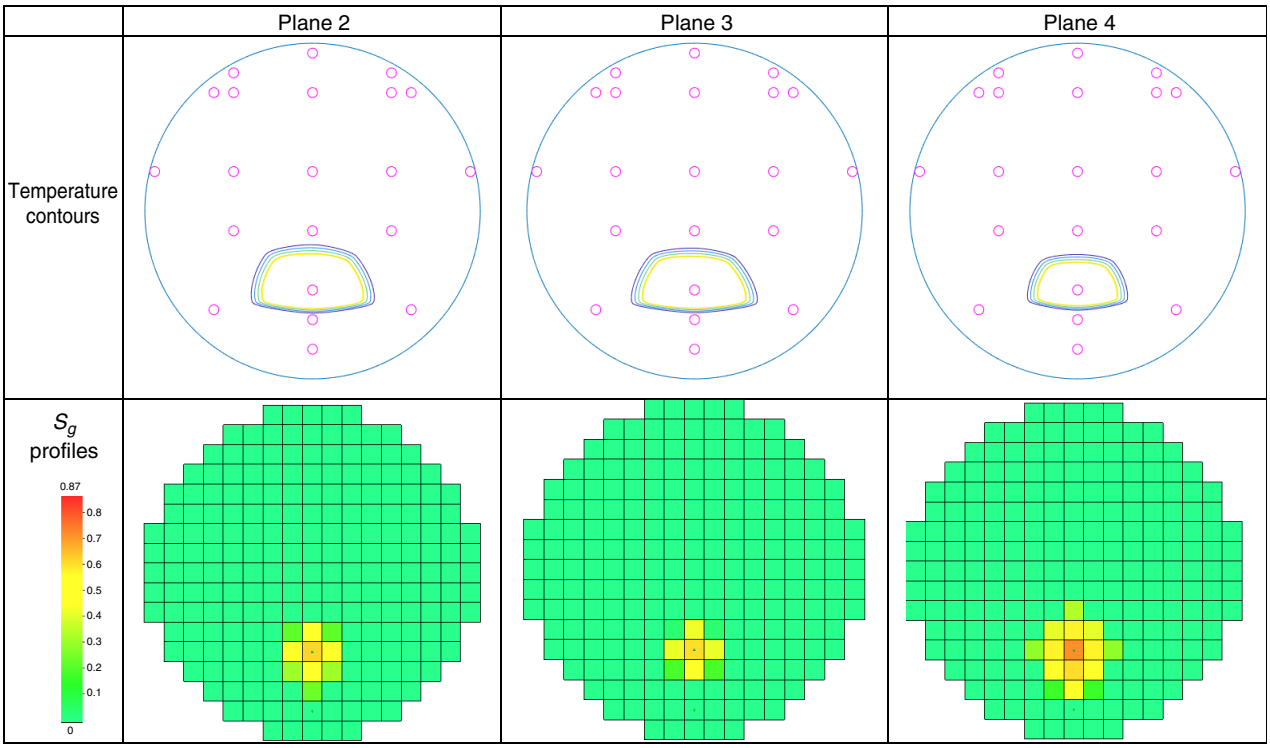

(a) Day 2

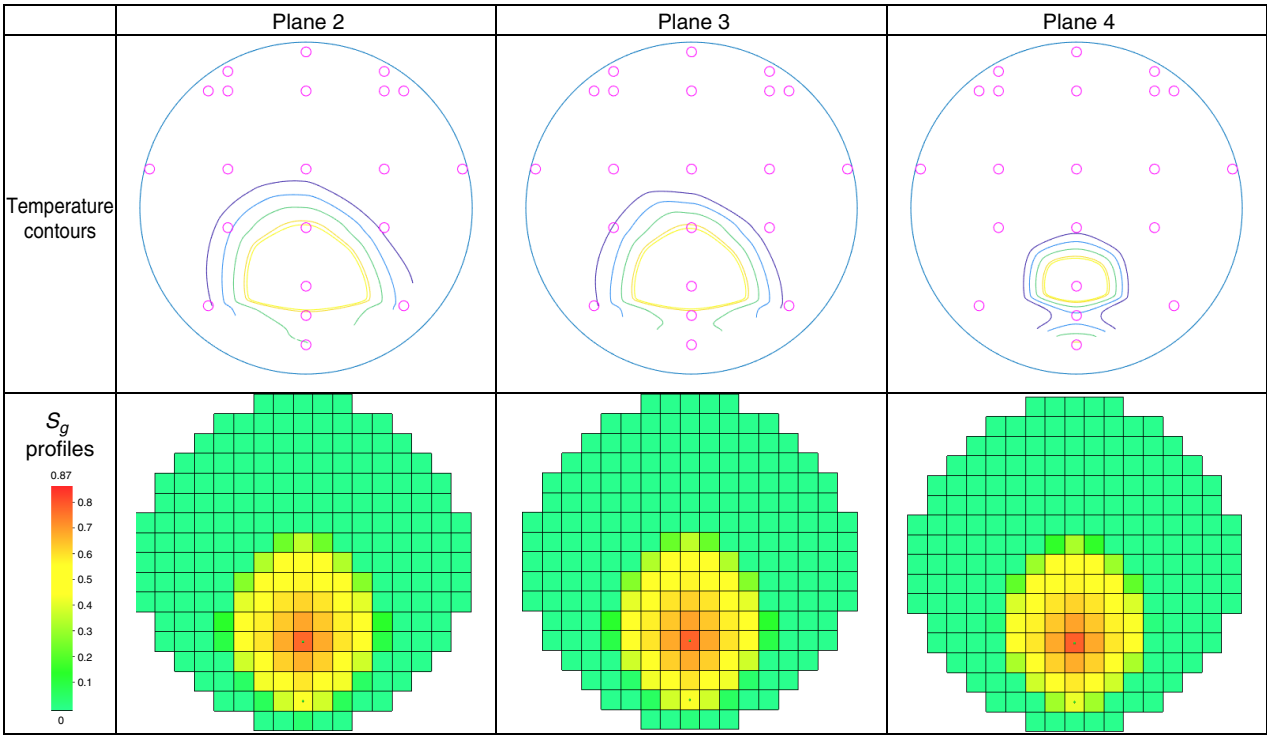

(b) Day 3

Fig. 6—The top columns show temperature contours from the SAGD experimental data. The contours represent the isotherms for 242°C, 240°C, 235°C, 230°C, and 225°C from the inside to the outside of the steam chamber. The bottom columns show the simulated gas saturation profiles.

Fig. 8 shows the temporal variation of asphaltene weight percentage and density of the 10 produced bitumen samples and the original bitumen. It shows that the asphaltene content was close to the original bitumen at the beginning and started decreasing when the steam chamber started expanding from day 3. By the end of the experiment, the produced bitumen sample contained 5-wt% less asphaltene than the original bitumen.

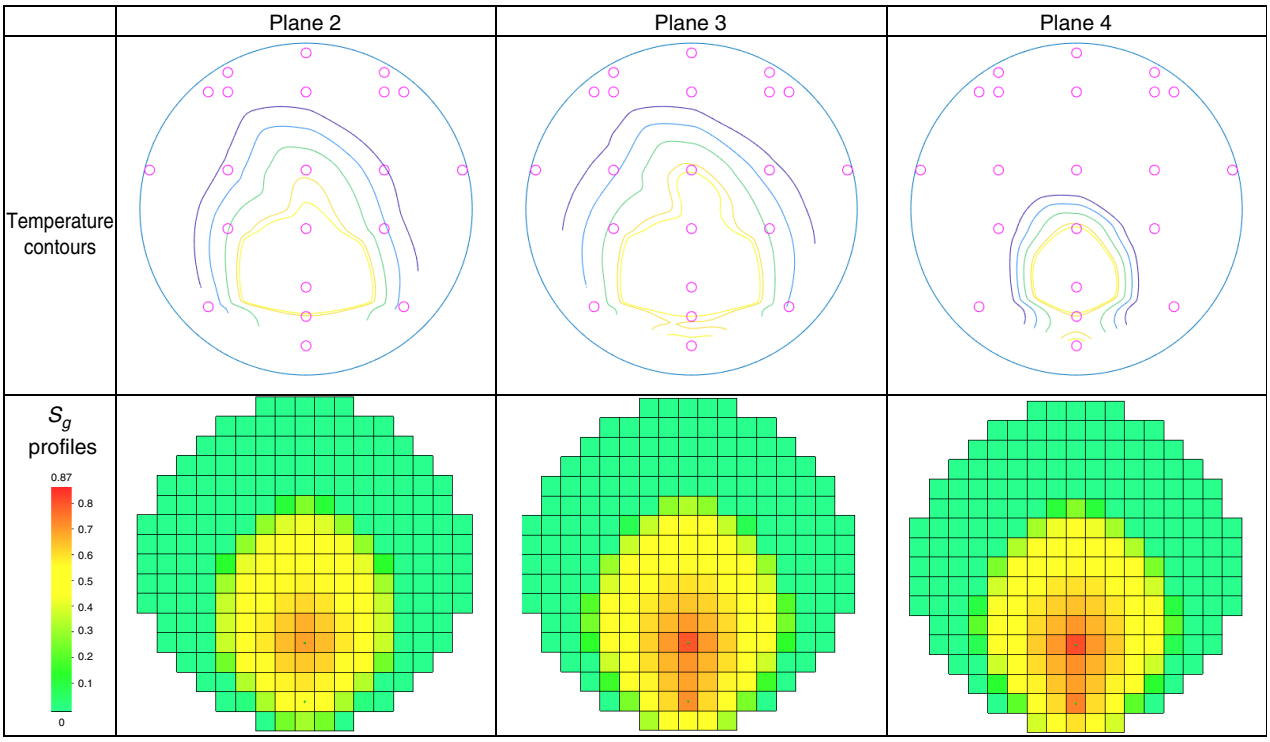

(c) Day 5

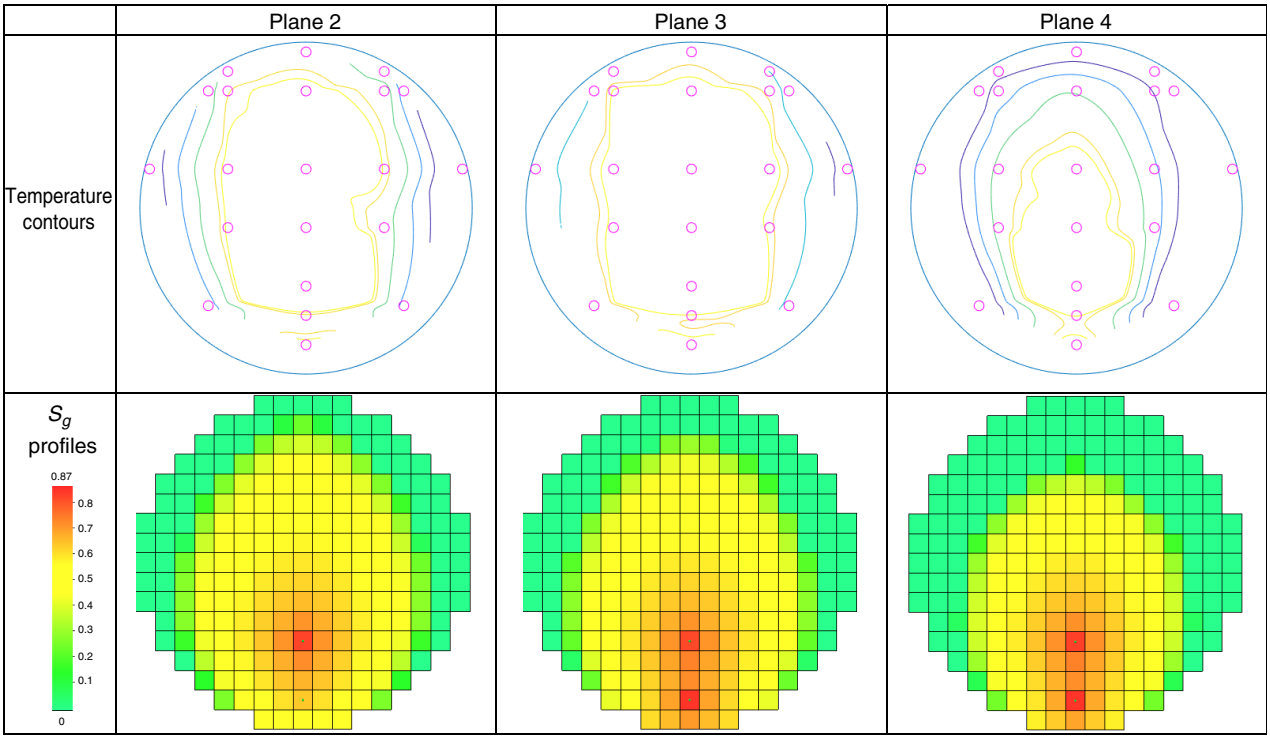

(d) Day 7

Fig. 6 (continued)—The top columns show temperature contours from the SAGD experimental data. The contours represent the isotherms for 242°C, 240°C, 235°C, 230°C, and 225°C from the inside to the outside of the steam chamber. The bottom columns show the simulated gas saturation profiles.

The produced bitumen density exhibits the same trend as shown in **Fig. 9**, in which the produced bitumen gradually became less dense. By the end of the experiment, the produced bitumen was approximately 6 kg/m^3 less dense than the original bitumen. This translates to an increase in API gravity from the original 7.9° to 8.6°. In the actual operations, bitumen is diluted with condensate to decrease the oil viscosity for pipeline shipping. This decrease in bitumen density along with viscosity will decrease the diluent cost by 5 to 10%; that is, it is important to study the factors affecting the produced bitumen density in the SAGD operations.

Time (minutes)	C_{11}–C_{50} (wt%)	Asphaltenes (wt%)	Density at 15°C (kg/m^3)	Density at 40°C (kg/m^3)	Density at 80°C (kg/m^3)
1,675	65.1	15.8	1012.77	998.14	973.01
2,235	65.1	16.1	1012.62	997.62	972.55
2,685	64.8	16.6	1013.56	998.44	973.33
3,090	65.5	16.9	1012.84	997.68	972.27
3,525	64.6	16.5	1012.48	997.28	971.90
3,975	65.3	16.3	1012.27	997.21	971.81
4,275	65.0	16.0	1012.29	997.31	972.13
4,875	65.3	15.4	1011.87	996.95	971.71
7,575	65.8	13.3	1010.60	996.72	972.23
10,455	66.1	12.6	1009.26	995.95	971.32

Table 3—Produced bitumen properties.

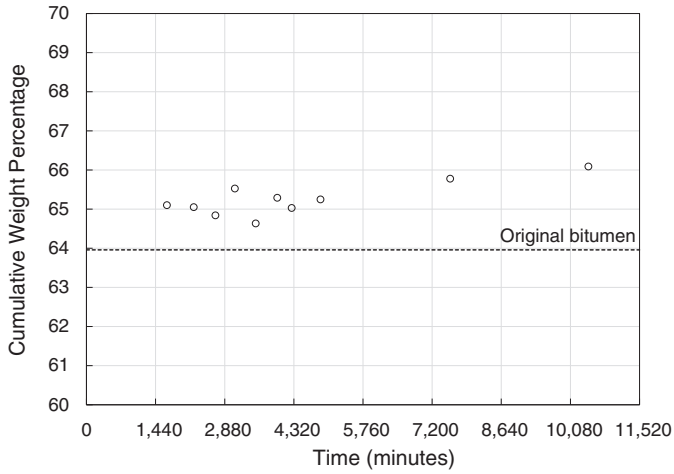

Fig. 7—Cumulative weight percentage from C11 to C50 for the 10 produced bitumen samples. The dashed line shows the original bitumen data as the reference.

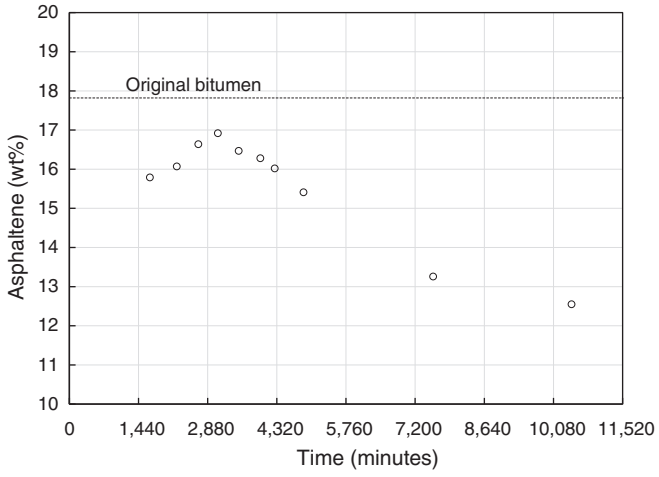

Fig. 8—Asphaltene weight percentage of the produced bitumen samples. The dashed line shows the original bitumen data as the reference.

The sandpack was excavated from both the injection and production sides. The two halves of the sandpack from the injection and production sides were divided into four segments. Segment 1 was closer to the flange, and Segment 4 was closer to the center of the coreholder **(Fig. 10).** Five locations were sampled on each of the eight segments, as indicated in Fig. 10. The successful samplings and measurements were reported in **Table 4.**

Whether each sampling location was swept by steam was analyzed to see if there is any correlation with the asphaltene content in the remaining oil. At certain segments (e.g., Segment 4 from the injection side), the steam chamber was estimated by the sand color: the gray region for the steam chamber and the brown region for the unswept region. Where the color was not distinctive, the steam chamber shape in Fig. 6 at the end of the experiment was also used to see if the sampling location was inside or outside of the steam

chamber. Planes 1 and 5 in Fig. 6 were close to the excavation Segments 1 from the injection and the production side, respectively. Planes 2 and 4 were close to Segments 3 from the injection and production sides, respectively. Plane 3 was close to excavation Segment 4. Table 4 summarizes the sampling locations based on our best effort. **Fig. 11** clearly shows that the asphaltene contents of remaining oil inside the steam chamber were greater than those outside the steam chamber. The original bitumen contained approximately 18-wt% asphaltene (Table 1), which indicates a reasonable cutoff between the data from inside and those from outside in Fig. 11. The result shows that the asphaltene content was approximately 1- to 7-wt% higher in the remaining oil inside the steam chamber in comparison to the original bitumen. The asphaltene content outside of the steam chamber remained similar to the original bitumen.

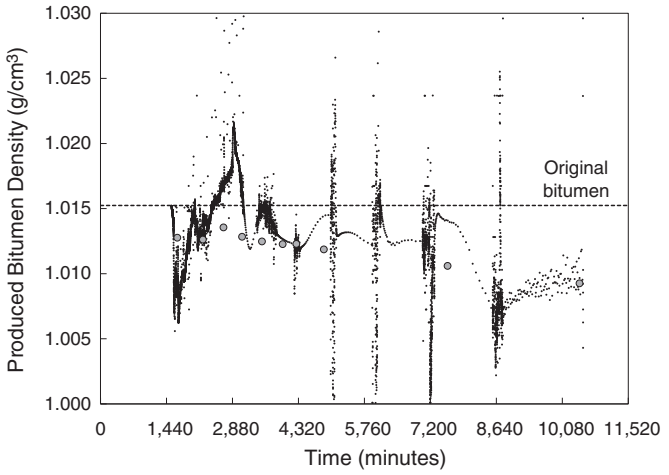

Fig. 9—Densities measured and simulated at 15°C for the produced bitumen samples. Gray dots are experimental data, and the dotted curves are simulated densities. The horizontal dashed line shows the original bitumen data as the reference.

Fig. 10—Photographs of the sandpack after the SAGD experiment. Four pictures at the top are on the injection side, and the four pictures at the bottom are on the production side.

History Matching and Analysis

Experimental results were history matched using the CMG STARS™ simulator (Computer Modelling Group 2018) with three-phase capillary pressures and two different sets of oil/water relative permeabilities for the early- and later-time domains. The initial stage of history matching identified the importance of matching temperature profiles as shown in Fig. 6, as indicated by an analytical theory of SAGD (Shi and Okuno 2018). It was also important to model varying flow regimes of oil and water as the steam chamber expanded. The basic steps of the history matching consisted of matching the temporal/spatial variation of the steam chamber by adjusting heat-loss parameters in time and space at the end of day 2 and the end of the SAGD experiment and matching the production history by adjusting relative permeability parameters according to the change in flow regime. Other parameters, such as the sandpack permeability/porosity, capillary pressures, and fluid properties, were determined before history matching and assumed constant during the SAGD experiment.

Sample No.	Asphaltene wt% of Oil	Inside/Outside Steam Chamber
	Injection side	
1	18.4	Inside
3	24.4	Inside
5	21.6	Unclear
6	18.6	Outside
9	18.1	Outside
10	16.6	Unclear
16	20.8	Inside
18	15.6	Outside
19	22.4	Inside
20	15.5	Unclear
	Production side	
1	17.4	Outside
3	19.3	Unclear
4	15.5	Outside
5	19.1	Unclear
6	17.3	Outside
7	15.1	Outside
9	19.5	Inside
10	16.6	Unclear
11	17.1	Outside
14	15.6	Outside
15	16.8	Unclear
16	16.1	Outside
17	18.6	Inside
18	16.1	Outside
19	18.1	Inside
20	17.8	Unclear

Table 4—Asphaltene wt% in the remaining oil after the SAGD experiment. “Unclear” means that the sampling location was half inside the steam chamber and half outside based on the chamber boundary shown in Fig. 6.

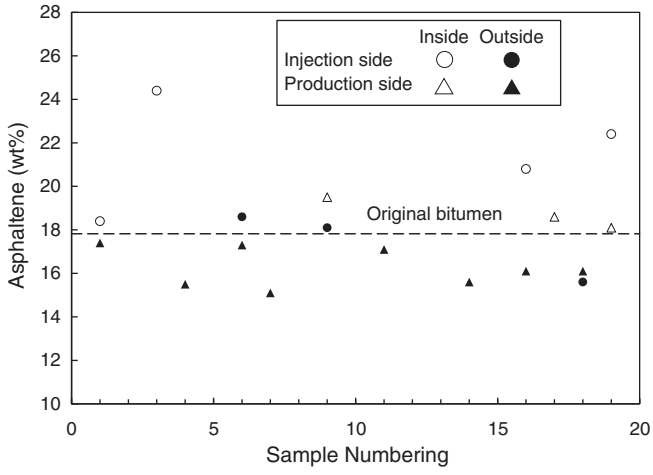

Fig. 11—Comparison of the asphaltene weight percentage in the remaining oil after the SAGD experiment and the original bitumen.

The sandpack was modeled as an approximate cylinder using rectangular gridblocks as shown in **Fig. 12.** There were 5,525 gridblocks in total for the sandpack model. It had 17 gridblocks for the diameter and 25 gridblocks along the wellbore. The dimensions of each gridblock were 0.025 m × 0.0488 m × 0.025 m ($I \times J \times K$), with the wellbore extending in the J-direction. Also, two vertical cross sections on the two ends of the sandpack represented the metal flanges. Although not shown in this paper, use of the sandpack model that was refined by a factor of 4 in the I-K planes did not change the discussion.

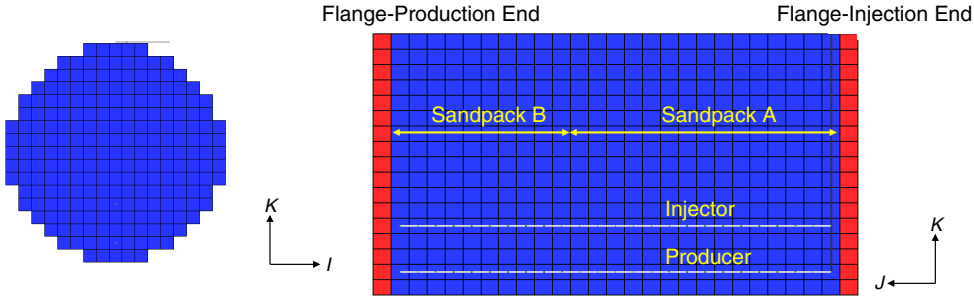

(a) Side view (b) Front view and thermal rock types

Fig. 12—Sandpack model and thermal rock types used for numerical simulation (thermal properties are given in Table 8).

The bitumen was characterized by the Peng-Robinson equation of state (PR EOS) with two pseudocomponents, a distillable component, B1, and a nondistillable component, B2. **Table 5** provides the PR EOS model. The bitumen densities and viscosities were measured and modeled as explained in Appendix A. **Tables 6 and 7** present the viscosity and density models used in STARS, respectively.

Component	Mol (%)	Molecular Weight (g/mol)	T_c (°C)	P_c (kPa)	Acentric Factor
B1	55.1	284.3	574.55	1890	0.4342
B2	44.9	892.9	1202.85	1230	1.0270

Table 5—PR EOS model for bitumen using two pseudocomponents. The binary interaction parameter between B1 and B2 is zero. T_c = critical temperature; P_c = critical pressure.

T (°C)	B1	B2
10	1.98×10^{1}	4.61×10^{12}
20	1.31×10^{1}	1.83×10^{11}
30	9.20	1.14×10^{10}
40	6.73	1.03×10^{9}
50	5.10	1.27×10^{8}
60	3.98	2.05×10^{7}
70	3.18	4.14×10^{6}
80	2.60	1.01×10^{6}
90	2.16	2.92×10^{5}
100	1.83	9.69×10^{4}
110	1.56	3.64×10^{4}
120	1.35	1.52×10^{4}
130	1.18	6.94×10^{3}
140	1.04	3.44×10^{3}
150	9.28×10^{-1}	1.83×10^{3}
160	8.32×10^{-1}	1.04×10^{3}
170	7.50×10^{-1}	6.20×10^{2}
180	6.80×10^{-1}	3.89×10^{2}
190	6.21×10^{-1}	2.55×10^{2}
200	5.69×10^{-1}	1.73×10^{2}
210	5.24×10^{-1}	1.22×10^{2}

Table 6 —Effective viscosities of B1 and B2 for the STARS simulator. They were calibrated using the experimental data given in the Appendix.

T (°C)	B1	B2
220	4.84×10^{-1}	8.87×10^{1}
230	4.50×10^{-1}	6.61×10^{1}
240	4.19×10^{-1}	5.06×10^{1}
250	3.92×10^{-1}	3.95×10^{1}
260	3.67×10^{-1}	3.15×10^{1}
270	3.45×10^{-1}	2.56×10^{1}
280	3.26×10^{-1}	2.11×10^{1}
290	3.08×10^{-1}	1.76×10^{1}
300	2.92×10^{-1}	1.50×10^{1}

Table 6 (continued)—Effective viscosities of B1 and B2 for the STARS simulator. They were calibrated using the experimental data given in the Appendix.

Component	ρ_{ref} (mol/m^3)	α_1 (K^{-1})	α_2 (K^{-2})	α_3 (kPa^{-1})	α_4 (kPa^{-1} K^{-1})
B1	2939.5	6.07×10^{-4}	9.24×10^{-7}	1.22×10^{-6}	4.16×10^{-9}
B2	1239.4	4.69×10^{-4}	7.48×10^{-8}	6.71×10^{-8}	2.17×10^{-10}

Table 7—Parameters for oil density for the STARS simulator. They were calibrated using the experimental data given in the Appendix.

The simulation was divided into two time domains. The first period included the preheating and the first day of steam injection without the heat-loss control for the bottom half of the sandpack. The second period was for the remaining 5 days with the bottom band heater on that decreased the heat losses. Each period required its own heat-loss parameters to account for the operational change of the bottom band heater.

The thermal conductivities of the sandpack, water, oil, and gas phases in the simulations were 1.23, 0.36, 0.072, and 0.02 *J*/(cm·min·°C), respectively. They were not adjusted for history matching. As indicated in **Table 8**, the level of heat losses varied in the sandpack with greater heat losses on the production side than on the injection side. Accordingly, the sandpack was divided into two thermal rocktypes as shown in Fig. 12b. It was set in the STARS simulation that the heat losses occurred in the *I*- and *K*-directions for the sandpack (sideways and over- and underburdens) and through the flanges in the *J*- and *K*-directions (along the directions of wellbore and over- and underburdens).

	Flange: Injection End	Flange: Production End	Sandpack A	Sandpack B
(a) Period 1: Bottom band heater off				
Heat conductivity in *I*, *J*/(cm·min·°C)	—	—	35.0	35.0
Heat capacity in *I*, *J*/(cm^3·°C)	—	—	35.0	35.0
Heat conductivity in *J*, *J*/(cm·min·°C)	0.5	2.0	35.0	35.0
Heat capacity in *J*, *J*/(cm^3·°C)	0.5	2.0	35.0	35.0
Heat conductivity in $+K$, *J*/(cm·min·°C)	0.2	0.2	35.0	35.0
Heat capacity in $+K$, *J*/(cm^3·°C)	0.02	0.2	35.0	35.0
Heat conductivity in $-K$, *J*/(cm·min·°C)	0.15	0.15	1.0	1.0
Heat capacity in $-K$, *J*/(cm^3·°C)	0.02	0.2	1.0	1.0
(b) Period 2: Bottom band heater on				
Heat conductivity in *I*, *J*/(cm·min·°C)	—	—	7.0	9.0
Heat capacity in *I*, *J*/(cm^3·°C)	—	—	1.0	1.0
Heat conductivity in *J*, *J*/(cm·min·°C)	0.5	2.0	—	—
Heat capacity in *J*, *J*/(cm^3·°C)	0.5	2.0	—	—
Heat conductivity in $+K$, *J*/(cm·min·°C)	0.2	0.2	1.0	2.0
Heat capacity in $+K$, *J*/(cm^3·°C)	0.02	0.2	1.0	2.0
Heat conductivity in $-K$, *J*/(cm·min·°C)	0.15	0.15	1.0	2.0
Heat capacity in $-K$, *J*/(cm^3·°C)	0.02	0.2	1.0	2.0

Table 8—Heat-loss parameters for history matching. *I*, *J*, $+K$, and $-K$ are the directions perpendicular to the well pair, along the well pair, underburden, and overburden, respectively.

Fig. 13 shows the capillary pressures for water/oil and oil/gas. They were calculated by the bundle-of-capillary-tube model. Pore diameters were calculated using the Carman-Kozeny equation with the grain-size distribution given in Fig. 4. The interfacial tensions for water/bitumen and steam/bitumen were assumed to be 30 and 15 dynes/cm, respectively. The rock surfaces were assumed to be strongly water-wet. The capillary pressures were considered in the simulation because the gravity and capillary forces were comparable

to each other in this sandpack experiment; for example, the gravity forces caused by a steam chamber can be several thousand Pascals, which is comparable to the capillary forces presented in Fig. 13. Consideration of capillary pressures was also necessary to model the mixed flow regimes of counter- and cocurrent flow of water and oil as will be discussed later.

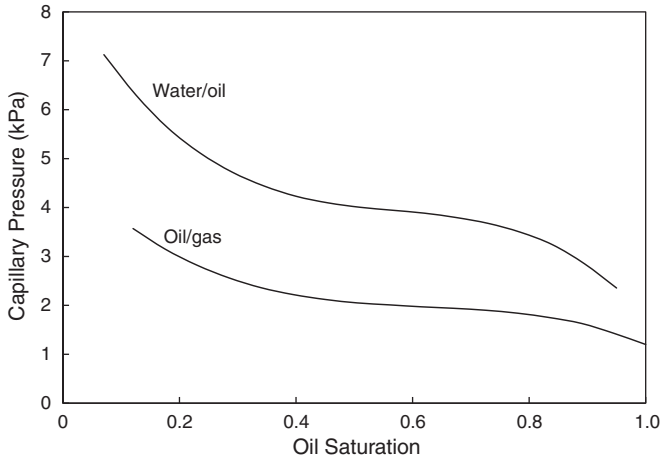

Fig. 13—Capillary pressure curves used for the History Matching and Analysis section. The assumed interfacial tension between oil and water is 30 dynes/cm and that between liquid and gas is 15 dynes/cm.

Figs. 5 and 6 compare the experimental data and the simulation results after history matching. Fig. 5 shows that the history-matched simulation with two time domains reasonably represents the cumulative injection and production curves. It was important to match the chamber expansion and the temperature profiles as shown in Fig. 6 as the first step of history matching. Planes 1 and 5 were not compared in Fig. 6 because the thermometers on those two planes were in contact with the metal flanges; therefore, the temperature readings were not indicative of the expansion of a steam chamber.

Fig. 14 and Table 9 show the relative permeabilities of the oil, water, and gas phases for Periods 1 and 2. The history matching required the relative permeabilities to be smaller in Period 1 than in Period 2. It is common practice in history matching to treat relative permeabilities in multiphase Darcy's law as empirical parameters that implicitly account for various factors that influence the phase mobilities. As described later, therefore, simulation results were analyzed for potential factors that decreased the relative permeabilities in Period 1.

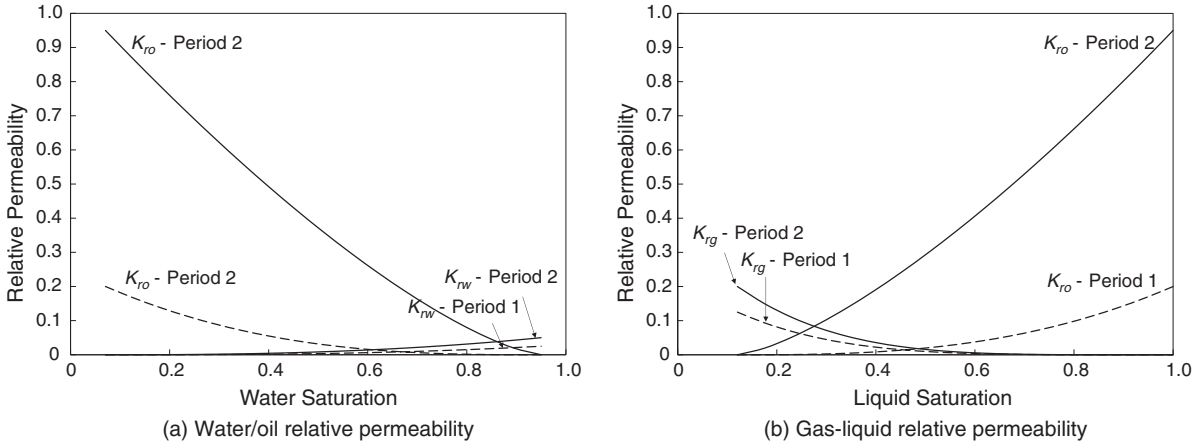

Fig. 14—Relative permeability models for the STARS simulation model in the History Matching and Analysis section. The liquid saturation was extended to 1.0 for the gas-liquid relative permeability model (b) because it improved the convergence of the STARS simulator.

Fig. 15 presents simulated profiles of phase saturations, pressures, fluxes, oil viscosity, and B1 concentration in the oil phase. The profiles at the end of Period 1 for Plane 2 are shown in the left column and those at day 5 (Period 2) are in the right column.

In the left column, the steam chamber has not expanded (Fig. 15a). The oil viscosity distribution shows that the region of mobile fluids is limited in the vicinity of the well pair, where the condensed water has accumulated (Figs. 15b and 15c). The increased water saturation around the well pair results in a gradient of capillary pressure between the oil and water phases (Fig. 15e). In the presence of a capillary pressure gradient, the multiphase flow of the oil and water phases in the sandpack tends to exhibit mixed flow regimes of counter- and cocurrent flow. The water phase pressure decreases from the steam chamber edge in the outward direction, whereas the oil phase pressure increases in the same direction (Figs. 15g and 15h). Figs. 15j and 15k indicate the directions of the water and oil fluxes by arrows and their magnitudes by colors. They show countercurrent flow of water and oil where the condensed water has accumulated above the well pair. There are high oil pressure and cocurrent flow near the sandpack's outer boundary because of thermal expansion; however, the oil viscosity in this region is too high to contribute to oil production (Fig. 15b). The oil production during Period 1 comes mainly from the countercurrent flow where water saturation is high.

	Period 1 (Bottom Band Heater Off)	Period 2 (Bottom Band Heater On)
S_{wr}	0.07045	0.07045
S_{or} (oil/water, oil/gas)	0.05	0.05
S_{gr}	0	0
$K_{ro}\,(S_w = S_{wr})$	0.20	0.95
$K_{rw}\,(S_w = 1 - S_{or})$	0.025	0.05
$K_{rg}\,(S_l = 1 - S_{gr})$	0.125	0.20
Exponent, K_{rw}	2.75	2.5
Exponent, K_{ro}	2.75	1.4
Exponent, K_{rg}	4.5	4.5

Table 9—Relative permeability parameters for the three-phase Stone-I model after history matching.

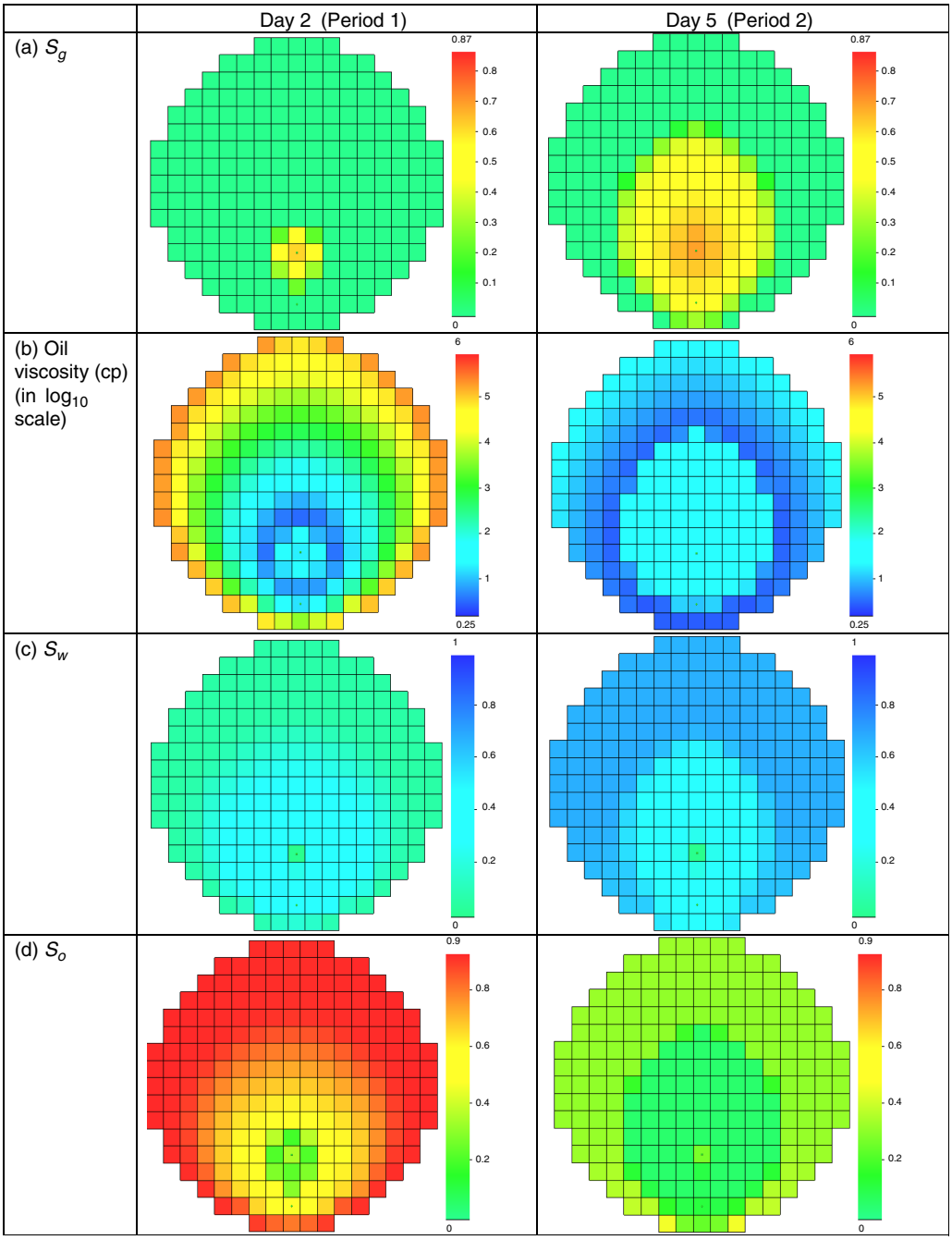

Fig. 15—Profiles of Plane 2 on the second (Period 1) and fifth day (Period 2) in the STARS simulation presented in the History Matching and Analysis section.

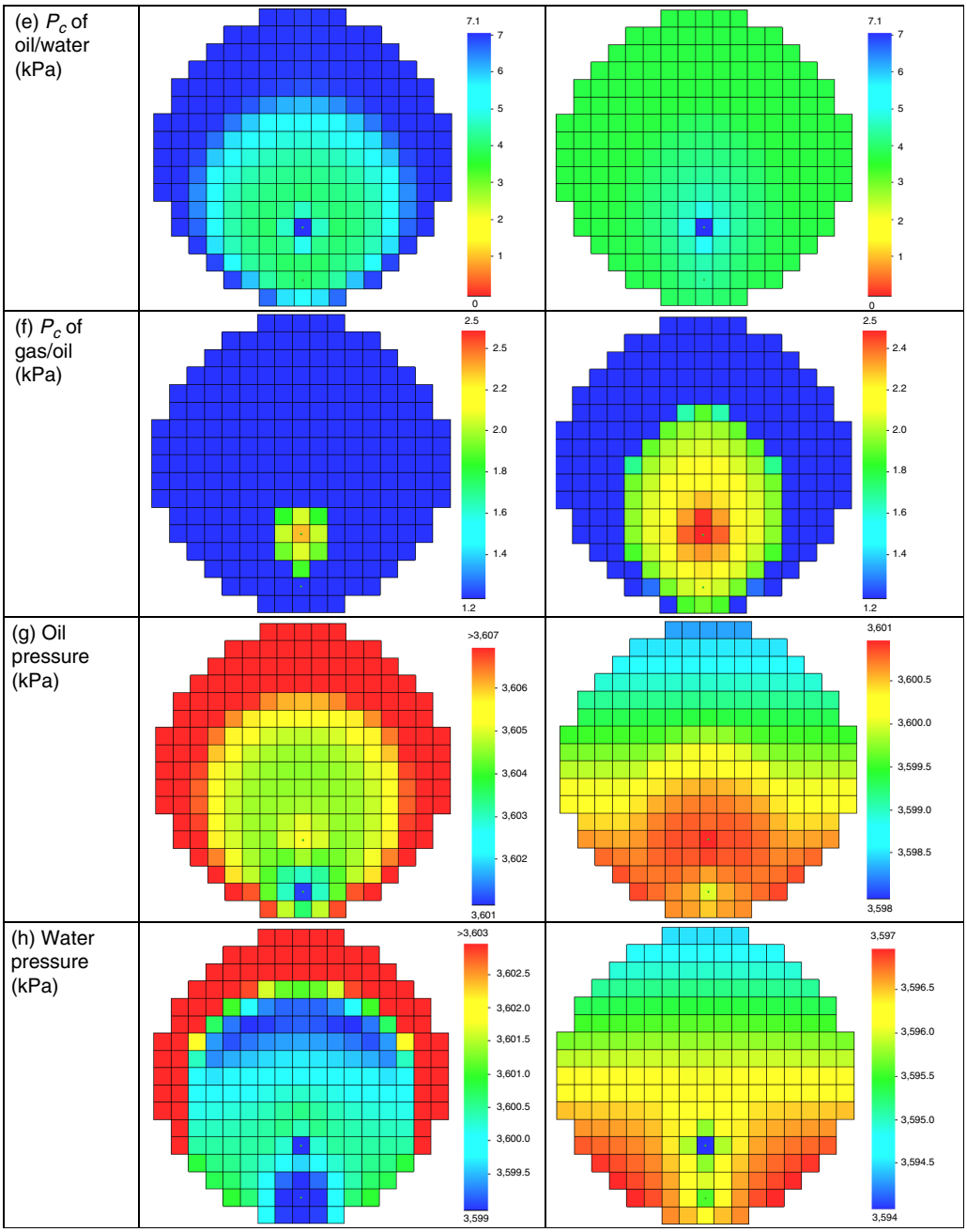

Fig. 15 (continued)—Profiles of Plane 2 on the second (Period 1) and fifth day (Period 2) in the STARS simulation presented in the History Matching and Analysis section.

In the right column of Fig. 15, the steam chamber expanded, and the oil viscosity decreased in the entire cross section (Figs. 15a and 15b). The oil and water phase saturations distribute more uniformly outside of the steam chamber (Figs. 15c and 15d) in comparison to the left column; therefore, the capillary pressure distributes more uniformly in Period 2 (Fig. 15e). Both oil and water pressures decrease with elevation. The multiphase flow of oil and water is predominantly cocurrent as shown in Figs. 15j and 15k.

Sensitivity analysis has indicated that simulations without considering capillary pressure significantly overestimate the rate for the steam rise and the size of the steam chamber when the bitumen recovery was history matched. Without considering capillary pressure, the simulation calculates that the oil and water phases flow cocurrently as they share the same pressure gradient. Also, using capillary pressure between oil and gas results in a thicker transition zone, which allows the steam chamber to expand both sideways and upwards as shown in Fig. 15.

The occurrence of countercurrent flow depends on the flow direction of the wetting phase, flow boundary, and viscosity ratio of the wetting and the nonwetting phases, among many other factors (Bourbiaux and Kalaydjian 1990; Kalaydjian 1990; Bentsen and Manai 1993; Haugen et al. 2015; Andersen et al. 2020). Based on the change in flow regime between Periods 1 and 2, the hypothesis behind using the different sets of relative permeabilities is that lower relative permeabilities were required at early times because the oil/water multiphase flow was affected by countercurrent flow with a small chamber and a large oil/water viscosity ratio.

Relative permeabilities are commonly determined using cocurrent flow data for two phases, which occurred only outside of the transition zone in the experiment. Data in the literature indicate that the relative permeabilities for countercurrent flow are lower than those for cocurrent flow because viscous coupling has an adverse effect on phase mobilities in countercurrent flow (Bourbiaux and Kalaydjian 1990; Kalaydjian 1990; Bentsen and Manai 1993). Several studies on three-phase flow in gravity drainage (Dehghanpour et al. 2011;

Dehghanpour and DiCarlo 2013; Murtaza et al. 2014) also showed that the viscous coupling of water, oil, and gas could be beneficial to oil drainage in the transition zone near a steam chamber edge where the cocurrent flow occurred. This may correspond to Period 2 in which a steam chamber was developed. Therefore, one set of relative permeabilities is not expected to describe the current SAGD experimental data, in which cocurrent and countercurrent flow likely occurred in different locations with varying relative magnitude over time. Further investigation is required into countercurrent flow and its impact on relative permeabilities at different stages of SAGD, which is beyond the scope of the current paper.

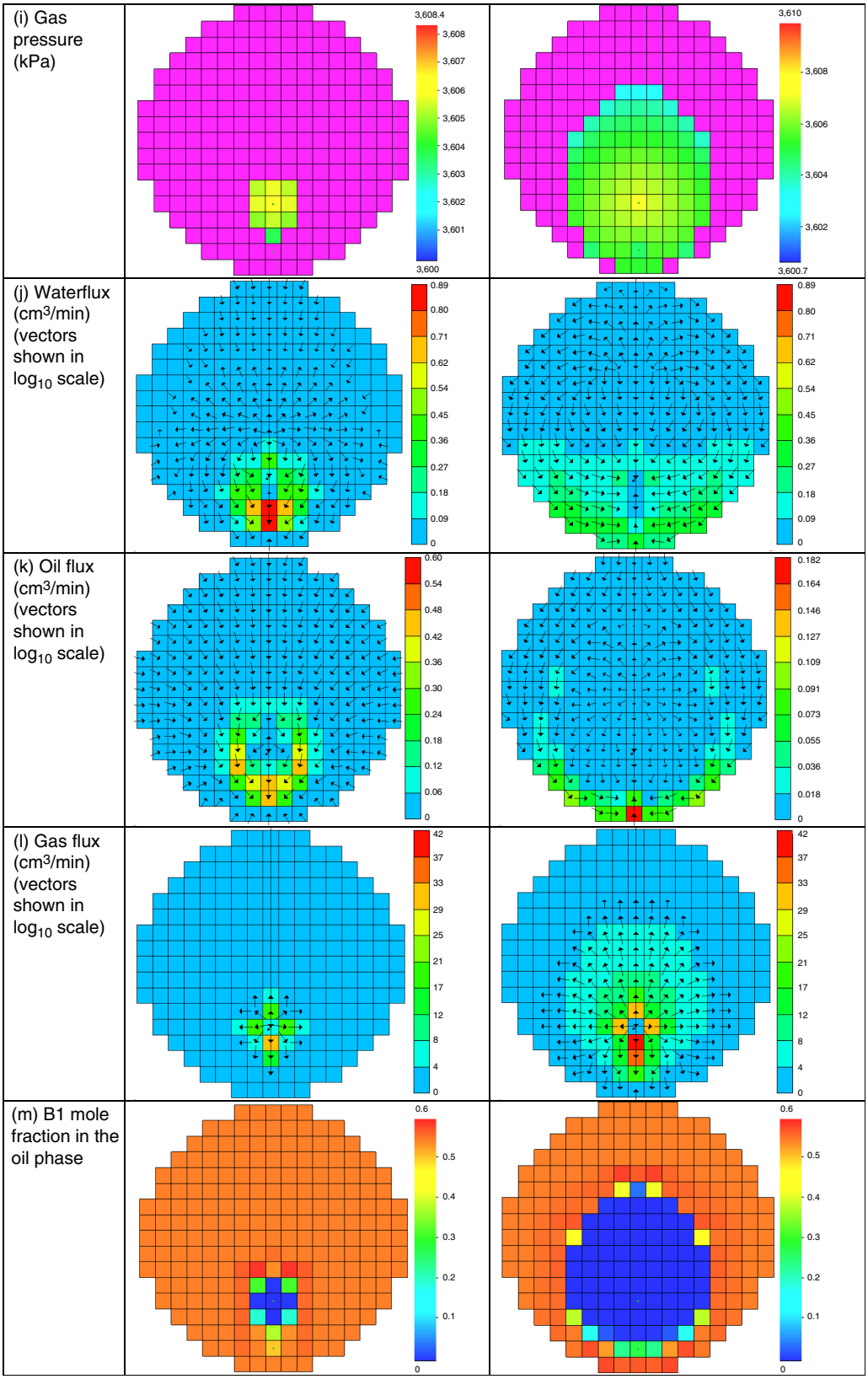

Fig. 15 (continued)—Profiles of Plane 2 on the second (Period 1) and fifth day (Period 2) in the STARS simulation presented in the History Matching and Analysis section

It has been shown in simulation studies (Ito and Hirata 1999; Kumar and Pooladi-Darvish 2002; Nasr et al. 2003; Walls et al. 2003) and measurements (Corey 1954; Asar and Handy 1988) that the endpoint relative permeability of gas can be lower than the wetting phase. Kumar and Pooladi-Darvish (2002) discussed that a low gas relative permeability was necessary to match heavy oil recovery driven by solution gas. Their observations were repeated in the current simulation model history matched with SAGD data as shown in Fig. 14b.

Results of the history-matched simulation show that the produced oil is lighter and the remaining oil in the sandpack is denser than the original bitumen, as observed in the experiment. Fig. 15m shows the B1 mole fraction in the simulation on the seconds and fifth days for Plane 2. The B1 concentration is high near the chamber edge but almost zero inside the steam chamber because of the distillation effect (Prats 1982; Keshavarz et al. 2015; Venkatramani and Okuno 2018). Light components in the remaining oil are vaporized and condensed near the chamber edge, resulting in the accumulation of the light components. Fig. 9 shows that the history-matched simulation represents the varying density of produced oil as observed in the experiment. In this figure, the fluctuations in the simulated density occurred when the producer was shut in to maintain the pressure inside the simulation model. The data and simulation indicated a larger amount of light components' distillation with increasing chamber volume, indicating the importance of properly matching the temporal/spatial variation of temperature. The accumulated light components near the chamber edge could be partly produced and therefore decrease the produced bitumen density.

Conclusions

We presented a large-scale experimental study of the distillation of the light-end bitumen components and its impact on the produced bitumen properties in SAGD. The experiment was conducted at 3,600 kPa and 244°C steam temperature, with a 5.6-darcy sandpack. The SAGD experiment was history matched by a numerical model in terms of temperature profiles (chamber growth) and oil and water production. The simulation was divided into two periods: Period 1 for the first two days (no bottom heater) and Period 2 for the rest of SAGD. The main conclusions are as follows:

- A compositional variation was observed in the produced bitumen for the SAGD experiment. The analysis of the produced bitumen showed an increase in components lighter than C_{50} by up to 2 wt% and a decrease in asphaltenes by up to 5 wt%, which led to a decrease in density up to 6 kg/m^3. This is an increase in API from the original value of 7.9° to 8.6°. This decrease in bitumen density will decrease the diluent cost by 5 to 10%; that is, it is important to study the factors affecting the produced bitumen density in the SAGD operations.
- The lighter produced bitumen likely resulted from the distillation of light components caused by the expansion of a steam chamber; that is, one of the in-situ upgrading mechanisms as defined by Ovalles (2019). Excavated sandpack samples showed that the remaining oil inside the steam chamber contained higher concentrations of asphaltenes than the original bitumen. The produced bitumen density also decreased as the steam chamber expanded. History-matched simulation results showed that the distillable B1 component partitioned into the vapor phase at high temperatures and condensed into the oil phase near the chamber edge, making the produced oil composition lighter than the original one.
- Capillary pressure had to be included in the simulation to obtain a reasonable match in terms of the bitumen production and the steam-chamber growth in SAGD. Without considering capillary pressure in the simulation, the expansion of a steam chamber is significantly overestimated even if the bitumen production history is matched. The inclusion of capillary pressure allows for different pressure gradients for different phases in simulation.
- The history-matched simulation indicated a transition in flow regime in the SAGD experiment that required two different sets of relative permeability curves for matching the bitumen recovery history in Periods 1 and 2. Countercurrent flow of water and oil was dominant when a steam chamber started to expand in Period 1, in which capillary-driven countercurrent flow contributed to the displacement of oil. Then, cocurrent flow of water and oil became dominant when the steam chamber had developed in the sandpack in Period 2. This transition in flow regime with an expanding steam chamber likely explains why smaller relative permeabilities at early times (Period 1) greatly improved the matching quality in terms of oil recovery history.

Nomenclature

kr = relative permeability
T = temperature, °C
P = pressure, kPa
xi = mole fraction of component i in the oil phase
α = fitting parameters for pure component density model in STARS
μ = viscosity, cp
ρ = density, kg/m^3

Acknowledgments

We gratefully acknowledge Japan Canada Oil Sands Ltd. and China National Offshore Oil Corporation International Ltd. for sponsoring this research. Ryosuke Okuno holds the Pioneer Corporation Faculty Fellowship in the Hildebrand Department of Petroleum and Geosystems Engineering at the University of Texas at Austin.

References

Al-Murayri, M. T., Maini, B. B., Harding, T. G.et al. 2016a. Cracked Naphtha Coinjection in Steam-Assisted Gravity Drainage. *Energy & Fuels* **30** (7): 5330–5340. https://doi.org/10.1021/acs.energyfuels.5b02773.

Al-Murayri, M. T., Maini, B. B., Harding, T. G. et al. 2016b. Multicomponent Solvent Co-Injection with Steam in Heavy and Extra-Heavy Oil Reservoirs. *Energy & Fuels* **30** (4): 2604–2616. https://doi.org/10.1021/acs.energyfuels.5b02774.

Andersen, P. Ø., Nesvik, E. K., and Standnes, D. C. 2020. Analytical Solutions for Forced and Spontaneous Imbibition Accounting for Viscous Coupling. *J Pet Sci & Eng* **186**: 106717. https://doi.org/10.1016/j.petrol.2019.106717.

Asar, H. and Handy, L. L. 1988. Influence of Interfacial Tension on Gas/Oil Relative Permeability in a Gas-Condensate System. *SPE Res Eval & Eng* **3** (1): 257–264. SPE-11740-PA. https://doi.org/10.2118/11740-PA.

Ayodele, O. R., Nasr, T. N., Beaulieu, G. et al. 2009. Laboratory Experimental Testing and Development of an Efficient Low Pressure ES-SAGD Process. *J Can Pet Technol* **48** (9): 54–61. https://doi.org/10.2118/09-09-54.

Bentsen, R. G. and Manai, A. A. 1993. On the Use of Conventional Cocurrent and Countercurrent Effective Permeabilities to Estimate the Four Generalized Permeability Coefficients which Arise in Coupled, Two-Phase Flow. *Transport Porous Media* **11** (3): 243–262. https://doi.org/10.1007/BF00614814.

Bourbiaux, B. J. and Kalaydjian, F. J. 1990. Experimental Study of Cocurrent and Countercurrent Flows in Natural Porous Media. *SPE Res Eval & Eng* **5** (3): 361–368. SPE-18283-PA. https://doi.org/10.2118/18283-PA.

Computer Modelling Group. 2018. *STARS Version 2018 User's Guide*. Calgary, Alberta, Canada: Computer Modelling Group.

Corey, A. T. 1954. The Interrelation between Gas and Oil Relative Permeabilities. *Producers Monthly* **19** (1): 38–41.

Dehghanpour, H., Aminzadeh, B., Mirzaei, M. et al. 2011. Flow Coupling during Three-Phase Gravity Drainage. *Phys Rev E* **83** (6): 065302. https://doi.org/10.1103/PhysRevE.83.065302.

Dehghanpour, H. and DiCarlo, D. A. 2013. A Comparative Study of Transient and Steady-State Three-Phase Oil Permeability. *J Can Pet Technol* **18** (1): 54–63. SPE-146603-PA. https://doi.org/10.2118/146603-PA.

Dong, L. 2012. Effect of Vapour–Liquid Phase Behaviour of Steam–Light Hydrocarbon Systems on Steam Assisted Gravity Drainage Process for Bitumen Recovery. *Fuel* **95**: 159–168. https://doi.org/10.1016/j.fuel.2011.10.044.

Duerksen, J. H. and Hsueh, L. 1983. Steam Distillation of Crude Oils. *SPE J*. **23** (2): 265–271. SPE-10070-PA. https://doi.org/10.2118/10070-PA.

Haddadnia, A., Zirrahi, M., Hassanzadeh, H. et al. 2018. Dimethylether—A Promising Solvent for ES-SAGD. Paper presented at the SPE Canada Heavy Oil Technical Conference, Calgary, Alberta, Canada, 13–14 March. SPE-189741-MS. https://doi.org/10.2118/189741-MS.

Haugen, Å., Fernø, M. A., Mason, G. et al. 2015. The Effect of Viscosity on Relative Permeabilities Derived from Spontaneous Imbibition Tests. *Transport Porous Media* **106** (2): 383–404. https://doi.org/10.1007/s11242-014-0406-4.

Hosseininejad Mohebati, M., Maini, B. B., and Harding, T. G. 2012. Experimental Investigation of the Effect of Hexane on SAGD Performance at Different Operating Pressures. Paper presented at the SPE Heavy Oil Conference, Canada, Calgary, Alberta, Canada, 12–14 June. SPE-158498-MS. https://doi.org/10.2118/158498-MS.

Ito, Y. and Hirata, T. 1999. Numerical Simulation Study of a Well in the Jacos Hangingstone Steam Pilot Project near Fort McMurray. *J Can Pet Technol* **38** (13): 1–11. PETSOC-99-13-38. https://doi.org/10.2118/99-13-38.

Ivory, J. J., Zheng, R., Nasr, T. N. et al. 2008. Investigation of Low Pressure ES-SAGD. Paper presented at the International Thermal Operations and Heavy Oil Symposium, Calgary, Alberta, Canada, 20–23 October. SPE-117759-MS. https://doi.org/10.2118/117759-MS.

Kalaydjian, F. 1990. Origin and Quantification of Coupling between Relative Permeabilities for Two-Phase Flows in Porous Media. *Transport Porous Media* **5** (3): 215–229. https://doi.org/10.1007/BF00140013.

Keshavarz, M., Okuno, R., and Babadagli, T. 2014. Efficient Oil Displacement near the Chamber Edge in ES-SAGD. *J Pet Sci & Eng* **118**: 99–113. https://doi.org/10.1016/j.petrol.2014.04.007.

Keshavarz, M., Okuno, R., and Babadagli, T. 2015. Optimal Application Conditions for Steam/Solvent Coinjection. *SPE Res Eval & Eng* **18** (1): 20–38. SPE-165471-PA. https://doi.org/10.2118/165471-PA.

Khaledi, R. R., Beckman, M. S., Pustanyk, K. et al. 2012. Physical Modeling of Solvent-Assisted SAGD. Paper presented at the SPE Heavy Oil Conference Canada, Calgary, Alberta, Canada, 12–14 June. SPE-150676-MS. https://doi.org/10.2118/150676-MS.

Kim, M., Abedin, A., Lele, P. et al. 2017. Microfluidic Pore-Scale Comparison of Alcohol- and Alkaline-Based SAGD Processes. *J Pet Sci & Eng* **154**: 139–149. https://doi.org/10.1016/j.petrol.2017.04.025.

Kumar, R. and Pooladi-Darvish, M. 2002. Solution-Gas Drive in Heavy Oil: Field Prediction and Sensitivity Studies Using Low Gas Relative Permeability. *J Can Pet Technol* **41** (3): 26–32. PETSOC-02-03-01. https://doi.org/10.2118/02-03-01.

Li, W., Mamora, D., and Li, Y. 2011. Light- and Heavy-Solvent Impacts on Solvent-Aided-SAGD Process: A Low-Pressure Experimental Study. *J Can Pet Technol* **50** (4): 19–30. SPE-133277-PA. https://doi.org/10.2118/133277-PA.

Liu, H., Cheng, L., Huang, S. et al. 2018. Evolution Characteristics of SAGD Steam Chamber and Its Impacts on Heavy Oil Production and Heat Consumption. *Int J Heat & Mass Transfer* **121**: 579–596. https://doi.org/10.1016/j.ijheatmasstransfer.2018.01.038.

Liu, P., Yuan, Z., Zhang, S. et al. 2018. Experimental Study of the Steam Distillation Mechanism during the Steam Injection Process for Heavy Oil Recovery. *J Pet Sci & Eng* **166**: 561–567. https://doi.org/10.1016/j.petrol.2018.03.096.

Mukhametshina, A. and Hascakir, B. 2014. Bitumen Extraction by Expanding Solvent-Steam Assisted Gravity Drainage (ES-SAGD) with Asphaltene Solvents and Non-Solvents. Paper presented at the SPE Heavy Oil Conference–Canada, Calgary, Alberta, Canada, 10–12 June. SPE-170013-MS. https://doi.org/10.2118/170013-MS.

Murtaza, M., He, Z., and Dehghanpour, H. 2014. An Approach To Model Three-Phase Flow Coupling during Steam Chamber Rise. *Can J Chem Eng* **92** (6): 1100–1112. https://doi.org/10.1002/cjce.21944.

Nasr, T. N., Beaulieu, G., Golbeck, H. et al. 2003. Novel Expanding Solvent-SAGD Process "ES-SAGD." *J Can Pet Technol* **42** (1): 13–16. PETSOC-03-01-TN. https://doi.org/10.2118/03-01-TN.

Ovalles, C. 2019. *Subsurface Upgrading of Heavy Crude Oils and Bitumen*. Boca Raton, Florida, USA: CRC Press.

Prats, M. 1982. *Thermal Recovery*. HL Doherty Memorial Fund, Vol. 7, Richardson, Texas, USA: Monograph Series, Society of Petroleum Engineers.

Sasaki, K., Akibayashi, S., Yazawa, N. et al. 1999. Experimental Modelling of the SAGD Process ¾ Enhancing SAGD Performance with Periodic Stimulation of the Horizontal Producer. Paper presented at the SPE Annual Technical Conference and Exhibition, Houston, Texas, USA, 3–6 October. SPE-56544-MS. https://doi.org/10.2118/56544-MS.

Sheng, K., Okuno, R., and Wang, M. 2018. Dimethyl Ether as an Additive to Steam for Improved Steam-Assisted Gravity Drainage. *SPE J*. **23** (4): 1201–1222. SPE-184983-PA. https://doi.org/10.2118/184983-PA.

Shi, X. and Okuno, R. 2018. Analytical Solution for Steam-Assisted Gravity Drainage with Consideration of Temperature Variation along the Edge of a Steam Chamber. *Fuel* **217**: 262–274. https://doi.org/10.1016/j.fuel.2017.12.110.

Venkatramani, A. and Okuno, R. 2018. Mechanistic Simulation Study of Expanding-Solvent Steam-Assisted Gravity Drainage under Reservoir Heterogeneity. *J Pet Sci & Eng* **169**: 146–156. https://doi.org/10.1016/j.petrol.2018.04.074.

Walls, E., Palmgren, C., and Kisman, K. 2003. Residual Oil Saturation inside the Steam Chamber during SAGD. *J Can Pet Technol* **42** (1): 39–47. PETSOC-03-01-03. https://doi.org/10.2118/03-01-03.

Willman, B. T., Valleroy, V. V., Runberg, G. W. et al. 1961. Laboratory Studies of Oil Recovery by Steam Injection. *J Pet Technol* **13** (7): 681–690. SPE-1537-G-PA. https://doi.org/10.2118/1537-G-PA.

Wu, C. H. and Brown, A. 1975. A Laboratory Study on Steam Distillation in Porous Media. Paper presented at the Fall Meeting of the Society of Petroleum Engineers of AIME, Dallas, Texas, USA, 28 September–1 October. SPE-5569-MS. https://doi.org/10.2118/5569-MS.

Xu, L., Abedini, A., Qi, Z. et al. 2018. Pore-Scale Analysis of Steam-Solvent Coinjection: Azeotropic Temperature, Dilution and Asphaltene Deposition. *Fuel* **220**: 151–158. https://doi.org/10.1016/j.fuel.2018.01.119.

Zirahi, A., Yamchi, H. S., Haddadnia, A. et al. 2020. 2-D Physical Model Experimental Study of Ethyl Acetate and Steam Co-Injection for In-Situ Bitumen Recovery. *Fuel* **265**: 116943. https://doi.org/10.1016/j.fuel.2019.116943.

Appendix A—Experimental Viscosity and Density Data for Bitumen

This appendix summarizes the measured bitumen properties used for the SAGD experiment and the simulation study. The measured viscosity and density data for the bitumen are summarized in Tables A-1 and A-2, respectively. The oil viscosity in STARS is calculated using the log-linear mixing of pure components:

$$\ln\mu_L = \sum_{i=1}^{Nc} x_i \ln\mu_i, \quad \text{(A-1)}$$

where μ_L is the oil phase viscosity, and μ_i and x_i are the viscosity and molar fraction of component i, respectively. The calibrated pure component viscosity is shown in Table 6. The calculated bitumen viscosity is compared with measured data in **Fig. A-1.** The average absolute deviation and the average absolute relative deviation of the reciprocal of the calculated bitumen viscosity are approximately 0.001 cp^{-1} and 6.8%, respectively.

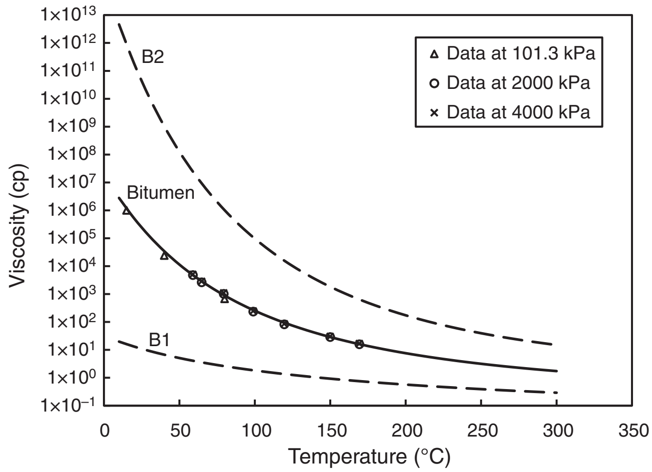

Fig. A-1—Comparison of bitumen viscosity calculated by the log-linear viscosity model in Table 6 and the measured data.

The oil phase density is calculated assuming ideal mixing of pure components in STARS:

$$1/\rho_L = \sum_{i=1}^{Nc} x_{iL}/\rho_{iL}, \quad \text{(A-2)}$$

where ρ_L is the molar density of oil phase, x_{iL} the mole fraction of component i in the oil phase, and N_C is the number of oil phase components. ρ_{iL} is the molar density of component i in phase j at T and P, which can be calculated as follows:

$$\rho_{iL} = \rho_{i\mathrm{ref}} \exp\left[-\alpha_1(T - T_{\mathrm{ref}}) - \frac{1}{2}\alpha_2\left(T^2 - {T_{\mathrm{ref}}}^2\right) + \alpha_3(P - P_{\mathrm{ref}}) + \alpha_4(P - P_{\mathrm{ref}})(T - T_{\mathrm{ref}})\right], \quad \text{(A-3)}$$

where P_{ref} is 101.3 kPa, T_{ref} is 15.56°C, and $\rho_{i\mathrm{ref}}$ is the molar density of component i at these conditions. α and $\rho_{i\mathrm{ref}}$ are regression parameters shown in Table 7. The calibrated density model is compared with data no greater than 6,000 kPa in **Fig. A-2.** The absolute deviation and average absolute relative deviation of calculated bitumen density are approximately 0.59 kg/m^3 and 0.1%, respectively.

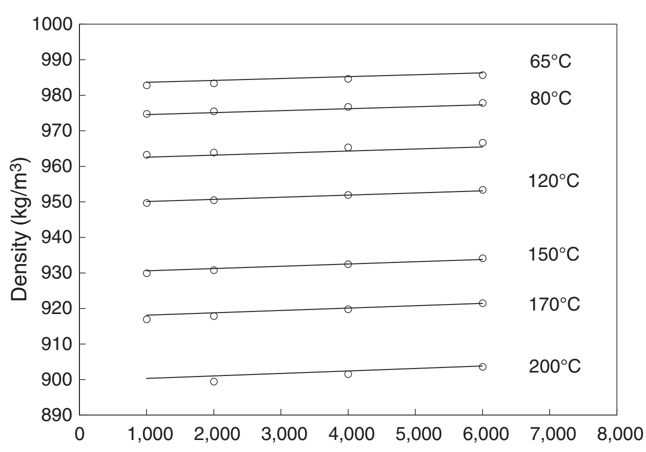

Fig. A-2—Comparison of bitumen density calculated by the STARS density model in Table 7 and the measured data.

Pressure (kPa)	Temperature (°C)						
	58.9	64.7	79.4	98.9	119.5	149.9	169.2
1,003	4,599	2,526	988.2	224.4	79.51	27.89	N/A
2,003	4,798	2,644	1,017	235.4	82.33	29.03	15.92
4,002	5,082	2,850	1,102	247.4	85.68	30.23	16.87
6,001	5,394	2,986	1,161	267.2	90.04	31.42	17.81
8,001	5,851	3,203	1,221	273.3	94.87	–	–
10,001	6,055	3,397	1,304	283.5	98.82	–	–

Table A-1—Experimental data for bitumen viscosities in this research. The conditions marked as "–" were not part of the experiment.

Pressure (kPa)	Temperature (°C)						
	66.5	81.0	100.0	119.9	151.0	170.9	199.3
1,002	982.79	974.76	963.25	949.70	929.92	916.95	N/A
2,002	983.35	975.48	963.88	950.49	930.78	917.85	899.41
4,001	984.59	976.72	965.32	951.94	932.47	919.77	901.53
6,003	985.67	977.86	966.64	953.37	934.15	921.49	903.58
8,004	986.73	979.02	967.90	954.75	935.74	923.23	905.54
9,999	987.85	980.26	969.20	956.17	937.26	924.99	907.41

Table A-2—Experimental data for bitumen densities in this research.